Dyes and Pigments 246 (2026) 113413

Contents lists available at ScienceDirect

Dyes and Pigments

journal homepage: www.elsevier.com/locate/dyepig

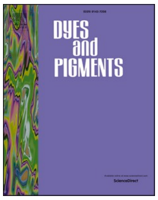

Anti-Kasha fluorescence for polarity detection in cellular compartments

Luis Crovetto [a], M. Paz Fernández-Liencres [b], Elena Villegas-Garcia [a], Jodie Henningway [c], M. Dolores Giron [d], Ramon Rios [c,e], Amparo Navarro [b,*], Jose M. Paredes [a,**]

[a] Nanoscopy-UGR Laboratory, Department of Physical Chemistry, Faculty of Pharmacy, Unidad de Excelencia en Quimica Aplicada a Biomedicina y Medioambiente (UEQ), University of Granada, Granada, 18071, Spain
[b] Departamento de Química Física y Analítica, Universidad de Jaén, Facultad de Ciencias Experimentales, Campus Las Lagunillas, 23071, Jaén, Spain
[c] School of Chemistry, University of Southampton, Highfield Campus, Southampton, SO17 1BJ, UK, Southampton, UK
[d] Department of Biochemistry and Molecular Biology II, Faculty of Pharmacy, University of Granada, Granada, 18071, Spain
[e] Department of Chemistry. Khalifa University. Abu Dhabi. UAE. Khalifa University of Science and Technology, P O Box 127788, Abu Dhabi, United Arab Emirates

ARTICLE INFO

Keywords:
Anti-Kasha
Ratiometric fluorescent sensor
Intracellular polarity
Fluorescence

ABSTRACT

This work explores the development, photophysical study, and application of a new fluorescent molecule based on BODIPY for sensing intracellular polarity which behaves as an unimolecular ratiometric probe. The experimental data show that the emission spectra of this molecule feature two distinct peaks in different solvents: one stable at 525 nm and another that shifts between 656 nm and 690 nm depending on the solvent polarity. Theoretical calculations using Density Functional Theory (DFT) and Time-Dependent DFT confirm the nature of these dual emission from the S_2 and S_1 excited states, respectively, and their sensitivity to solvent polarity. The study demonstrates that this molecule exhibits anti-Kasha fluorescence, which can be tuned by the surrounding environment, making it a potential tool for polarity sensing. The application of this compound in live cells shows its rapid uptake and ability to differentiate between various cellular compartments based on different polarity, using the S1/S2 ratio from the two emission channels. This research provides valuable insights into the development of efficient and specific fluorescent probes for visualizing and monitoring intra-cellular polarity contributing to advancements in cellular biology and medicine.

1. Introduction

Fluorescence-based techniques are widely recognized as a powerful approach for investigating the structure and functionality of biological materials [1]. These methods enable researchers to visualize physiological processes with high temporal and spatial resolution [2,3], detect multiple signals simultaneously, track single molecules in vivo [4,5], and study various pathological processes that would otherwise be challenging to observe [3,6,7]. Fluorescent probes are essential tools for studying biological systems. Their effectiveness relies on features such as low toxicity, strong detection capability, and excellent sensitivity, making them widely used in various applications today [8–10]. In contrast to non-fluorescent dyes, fluorescent probes exhibit high selectivity, as their activation or deactivation often depends on the surrounding biological environment [11,12]. Additionally, they can be excited at specific wavelengths and emit at wavelengths distinct from those of naturally fluorescent biomolecules, such as aromatic amino acids and NADH, minimizing background interference and enhancing detection sensitivity [13]. Fluorescent probes are widely employed to study membrane morphology by selectively binding to cellular membranes [14]. They are also used to label specific ligands, facilitating the investigation of conformational changes in proteins [13] and cellular signaling pathways [1]. Nevertheless, the development of fluorescent probes is challenging due to the structural complexity required to optimize key factors such as excitation wavelength, image resolution, bio-stability, and photo-stability. Despite these limitations, fluorescent probes continue to show great potential for future advancements in the field [15,16].

Polarity is a fundamental property of intracellular environments [17] and has been recognized as a key factor in various pathological processes, such as diabetes [18] and carcinogenesis [19]. Consequently, the ability to monitor and quantify polarity in real time within living cells is highly valuable, providing new opportunities to advance biomedical research. Although several fluorescent molecules currently function as

---

* Corresponding author.
** Corresponding author.
E-mail addresses: anavarro@ujaen.es (A. Navarro), jmparedes@ugr.es (J.M. Paredes).

https://doi.org/10.1016/j.dyepig.2025.113413
Received 8 September 2025; Received in revised form 3 November 2025; Accepted 12 November 2025

polarity sensors [11,20–25], there is a continuous demand for the development of more efficient, sensitive, and selective probes. In this context, polarity-sensitive ratiometric fluorescence probes have been designed in which the donor-acceptor structure allows ratiometric fluorescence emission dependent polarity [26]. Furthermore, the presence of both Kasha and anti-Kasha emission from a single fluorophore has opened the possibility to develop new ratiometric analysis strategies and there are still few studies in the literature that have addressed such unique emissive systems [27,28]. This methodology has been applied in the ratiometric quantification of cysteine and glutathione in living cells using the ratio between the S_2 and S_1 emission (S_2/S_1) taking the S_1 emission as internal reference signal [29]. While some fluorophores exhibiting anti-Kasha emission have been explored for polarity sensing, they either rely on variations in excitation and emission wavelengths [27] or do not exhibit a linear response to polarity [30]. To the best of our knowledge, no previous study has described a system utilizing linear polarity emission ratiometry, where a single excitation wavelength is used to obtain a polarity-sensitive Kasha emission band from the S_1 excited state alongside an invariant anti-Kasha emission band from the S_2 excited state.

In this context, we designed and synthesized a new fluorescent molecule based on 4-bora-3a,4a-diaza-*s*-indacene, commonly known as BODIPY (Boron-Dipyrromethene). BODIPYs represent an important family of organic dyes [31,32], characterized by excellent optical properties [33], including broad absorption across the visible spectrum, high molar extinction coefficients, high quantum yields, low cytotoxicity in the absence of irradiation (except for iodinated derivatives), remarkable resistance to oxidation, exceptional photostability, strong resistance to acidic and basic conditions, ease of synthesis, and structural tunability [34,35]. As a result, they have found applications in various fields, particularly in the life sciences [32,36].

Building on the aforementioned background, the main objective of this study is to investigate the photophysical properties of the new fluorescent molecule N-(2-((tert-butildimethylsiloxy)ethyl)-4-((E)-2-((E)-3-((E)-3-(5,5-difluoro-3,7-dimethyl-5H-4|4,5|4-dipyrrolo[1,2-c:2′,1′-f] [1–3]diazaborin-10-yl)allyliden)-5,5-dimethylcyclohex-1--en-1-yl)vinyl)-N-ethylaniline, (Compound **1**) shown in Scheme 1, and assess its suitability as an intracellular polarity sensor. Time-Dependent Density Functional Theory (TD-DFT) calculations have been key to interpreting the photophysical properties of this intriguing system and have allowed us to interpret the dual emission from two excited electronic states depending on the polarity of the solvent. By doing so, this work aims to contribute to the development of more efficient and specific tools for visualizing and monitoring intracellular polarity, which could, in turn, facilitate advancements in cellular biology and medicine.

2. Experimental section

2.1. Synthesis of compound 1

Compound **1** were obtained by the knovenagel reaction between aldehyde [37,38] and BODIPY [39], synthesized following known procedures, in 10 % yield as is presented in Scheme 1.

2.2. Sample preparation and spectroscopic measurements

All solvents were obtained from Sigma-Aldrich (Madrid, Spain). Stock solutions of compound **1** (3×10^{-4} M) were prepared in DMSO and 1,4-dioxane, then aliquoted and diluted in various solvents or solvent mixtures (DMSO, 1,4-dioxane, and water) to achieve the desired final concentration.

Fluorescence emission spectra under steady-state conditions were recorded using a Jasco FP-8300 spectrofluorometer (Jasco, Tokyo, Japan). UV–visible absorption measurements were performed with a Cary 60 UV–visible spectrophotometer (Agilent, Santa Clara, CA). Both instruments were equipped with a temperature control system to ensure stable experimental conditions (25 °C).

Fluorescence lifetime measurements were carried out using time-correlated single-photon counting (TCSPC) on a FluoTime 200 system (PicoQuant GmbH, Berlin, Germany). Excitation was provided by a pulsed diode laser (LDH-470, $\lambda_{ex} = 470$ nm) operating at a repetition rate of 20 MHz. Three emission decays were collected at 520−530 nm and 640–660 nm range for the Anti-Kasha and Kasha bands respectively for each solvent, using 1320 channels with a resolution of 37 ps per channel. Instrument response functions (IRFs) were recorded using a LUDOX scatterer, and both IRFs and sample decays were acquired until the peak channel reached 20,000 counts. The decay curves were analyzed globally using iterative reconvolution with multi-exponential fitting models implemented in the FluoFit software package (PicoQuant).

2.3. Microscopy measurements and image analysis

Live-cell microscopy imaging of compound **1** was performed using an Abberior scanning microscope (Abberior Instruments GmbH, Göttingen, Germany) equipped with a 485 nm pulsed excitation laser (40 MHz). A 100X UPlanSApo oil immersion objective (1.4 NA) was employed for image acquisition. The pinhole diameter was consistently

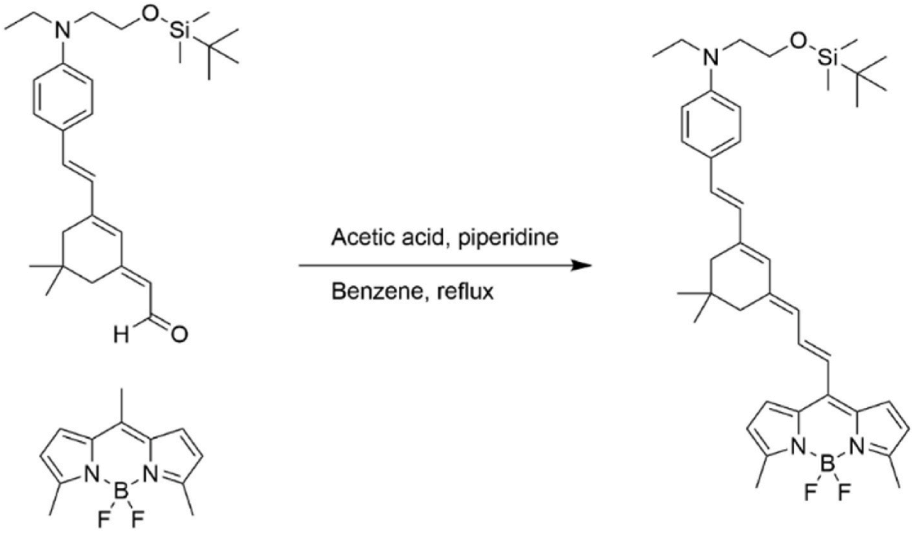

Scheme 1. Synthesis of compound 1.

adjusted to 1 Airy unit (AU) across all measurements. Fluorescence emission was separated by a 560LP dichroic mirror and directed toward two detection systems: an avalanche photodiode (APD) and a hybrid photomultiplier tube (HPMT). Before reaching the detectors, the emitted fluorescence was filtered through 509/11 nm (Green channel) and 685/75 nm (Red channel) bandpass filters into the APD and HPMT, respectively.

Cells were maintained in Dulbecco's Modified Eagle Medium (DMEM; Sigma-Aldrich, St. Louis, MO, USA) supplemented with 10 % heat-inactivated fetal bovine serum (FBS) (BioWhittaker, Lonza, Basel, Switzerland), 1 % L-glutamine, 2.7 % sodium bicarbonate, 1 % Hepes buffer, and 1 % penicillin/streptomycin solution (10,000 U mL^{-1} penicillin G and 10 mg mL^{-1} streptomycin; Sigma-Aldrich, St. Louis, MO, USA). The cultures were incubated at 37 °C in a humidified environment containing 5 % CO_2. For microscopy studies, cells were seeded onto μ-slide 8-well IbiTreat plates at a density of 5-11 × 10^4 cells per well. Prior to imaging, cultures were rinsed twice with PBS, followed by the addition of an aliquot of the stock solution in DMSO to PBS. The work solutions have a final DMSO concentration of 1.3 %

Image analysis was performed using Fiji (ImageJ) software with custom macros [40]. Initially, raw images were imported, and a Gaussian smoothing filter with a standard deviation of 0.5 pixels was applied. The entire cell was selected as the region of interest (ROI) and semi-automatically defined to generate binary masks, assigning a value of 0 to the background and 1 to the entire cell bodies. The images from both fluorescence channels were subsequently multiplied by the ROI, ensuring that only cellular regions remained in the processed images. To assess intracellular polarity, a ratiometric image was generated by dividing the red and green fluorescence intensities. Additionally, specific intracellular compartments were manually selected based on intensity thresholding, resulting in the analysis of five distinct internal structures.

2.4. Computational details

Density Functional Theory (DFT) calculations were performed to tackle full geometry optimization of the molecular geometry of the ground state and excited state was performed using the Gaussian 16 (revision A.03) suite of programs [41]. Since there is no data on the experimental geometry of compound **1**, two global hybrids functionals and two range-separated hybrids functionals were used with different fraction of Hartree-Fock exchange (HF), PBE0 (25 % HF) [42], M06-2X (54 % HF) [43], CAM-B3LYP (19 % at the short range and 65 % at the long range) [44] and ωB97XD (22 % at the short range and 100 % at long range) [45] in combination with 6-31+G** basis set. The vibrational frequencies were computed in the ground state and excited states being all real. The solvent was treated implicitly using the Polarizable Continuum Model (PCM) [43,46–48]. Time-Dependent DFT calculations (TD-DFT) using TD-PBE0, TD-M06-2X, CAM-B3LYP and ωB97XD functionals and 6-31+G** basis set were performed to calculate the vertical electronic transitions. The theoretical emission in solution was calculated as the difference $E(S_1/S_1)$ - $E(S_0/S_1)$ where $E(S_1/S_1)$ is the energy of the S_1 excited state at its equilibrium geometry (using both state-specific solvation approach (SS) [49] and $E(S_0/S_1)$ is the energy of the S_0 ground state at the S_1 excited state geometry and with the static solvation from the excited state [50].

3. Results and discussion

3.1. Photophysical study in solution

Fig. 1 presents the absorption spectrum of compound **1**, which exhibits a broad band in the 540–750 nm range across the studied solvents: 1,4-dioxane, DMSO, and water. In both DMSO and water, this band extends further, featuring a shoulder that approaches 800 nm. Additionally, multiple absorption peaks appear at shorter wavelengths in all solvents, corresponding to the complex absorption band between 300 and 450 nm. The absorption maxima are summarized in Table 1: 310, 360, and 560 nm in water; 310, 354, and 550 nm in DMSO; and 305, 384, and 540 nm in 1,4-dioxane. Notably, the lowest-energy (540–750 nm) band undergoes a bathochromic shift with increasing solvent polarity, whereas the higher-energy bands exhibit a negligible shift under the same conditions.

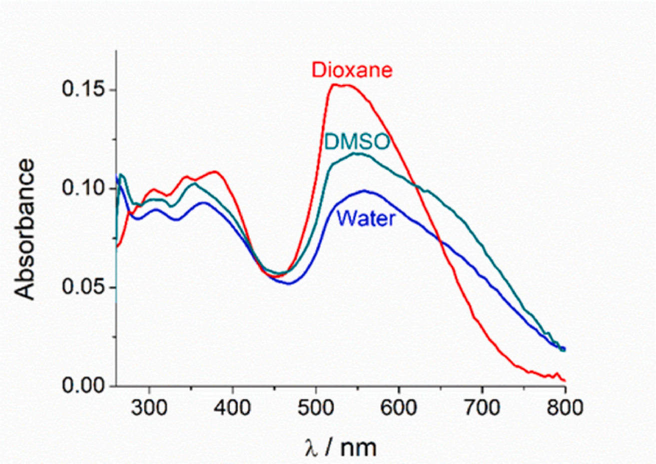

Fig. 1. Experimental absorption spectra of compound 1 (4 × 10^{-5} M) in dioxane, DMSO and water solution.

Next, the excitation and emission fluorescence spectra of compound **1** were recorded in the three selected solvents, as shown in Fig. 2A and B. The emission spectra exhibit two distinct peaks: one centered at 525 nm (green emission), which remains consistent across all solvents, and a second peak (red emission) that is clearly observed only in 1,4-dioxane. In DMSO, this second peak undergoes a blue shift and appears as a shoulder of the primary emission peak, whereas in water, it is entirely absent.

To elucidate the absorption transition bands, excitation spectra measurements were performed at two emission wavelengths (655 nm and 560 nm). This approach allows the identification of the absorption bands responsible for these distinct emissions.

The excitation spectra corresponding to the first emission band (centered at 525 nm) in the three solvents are presented in Fig. 2C. As shown, the spectra exhibit an intense excitation band at 514 nm in 1,4-dioxane, 513 nm in DMSO, and 508 nm in water. Conversely, excitation of the emission centered at 655 nm reveals excitation bands at 446 nm in 1,4-dioxane and 528 nm in DMSO. However, in water, this band is absent, rendering the fluorescence of compound **1** almost negligible (see Fig. 2D).

Our results indicate that compound **1** exhibits two distinct pairs of excitation-emission bands. The first pair, centered around 510/525 nm, remains relatively stable across all three solvents. In contrast, the second pair varies significantly, with excitation-emission bands at 447–650 nm in 1,4-dioxane, 527–615 nm in DMSO, and negligible emission in water.

Using an excitation wavelength of 470 nm, we excited both emission bands, resulting in a double-band emission in 1,4-dioxane (see Fig. 2A) and DMSO. However, since the red emission is negligible in water, only the green emission band is observed in this solvent. The selecion of this excitation wavelenght provides a strategic balance: it efficiently excites

Table 1
UV/vis and photoluminescence data (PL) of compound 1.

Solvent, dielectric constant (ε)	E^{exp}_{ab}/nm	E^{exp}_{em}/eV(nm)	Φ_F (%)
1,4-Dioxane, ε = 2.2	305, 384, 540	525, 655	44.42
DMSO, ε = 46.826	310, 354, 550	525, 620, 670	37.84
Water, ε = 78.3553	310, 360, 560	525	18.09

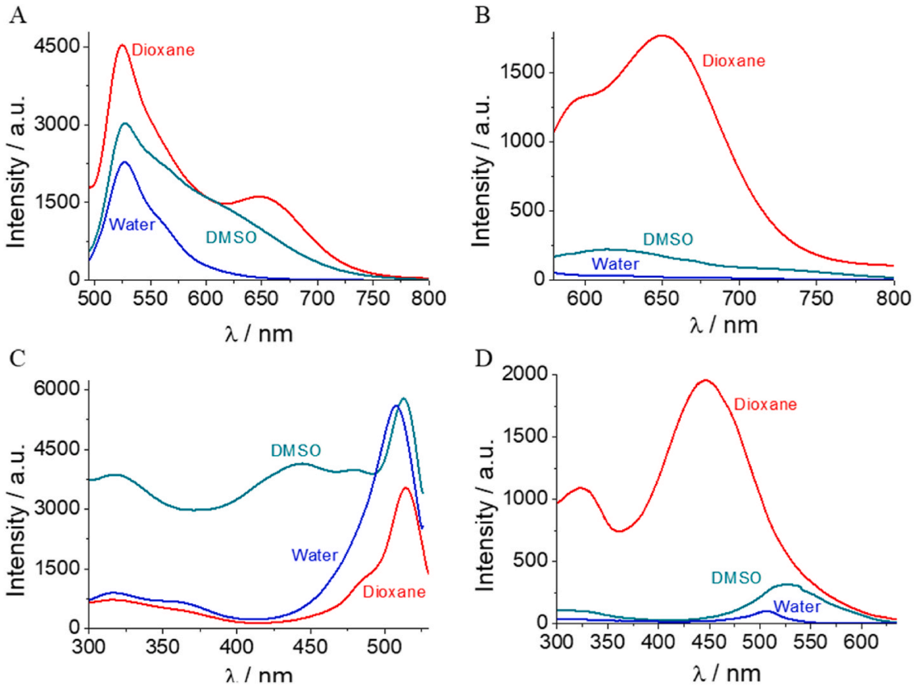

Fig. 2. Experimental fluorescence emission and excitation spectra of compound **1** (4×10^{-6} M) in dioxane, DMSO and water solution at the wavelength of A) emission spectra ($\lambda_{ex} = 470$ nm), B) emission spectra ($\lambda_{ex} = 560$ nm), C) excitation spectra ($\lambda_{em} = 540$ nm) and D) excitation spectra ($\lambda_{em} = 655$ nm).

both excitation bands, ensuring a simultaneous double emission bands for accurate ratiometric analysis.

Conversely, excitation at 560 nm preferentially excites the red emission band (see Fig. 2D), as the green emission band exhibits minimal excitation at this wavelength. The spectra in Fig. 2B indicate that compound **1** is nearly non-fluorescent in water. In 1,4-dioxane, the most apolar solvent tested, fluorescence intensity is high, whereas in DMSO, the emission undergoes a blue shift and exhibits reduced intensity compared to 1,4-dioxane. Notably, the solvent effect on the red emission band (650 nm in 1,4-dioxane, 615 nm in DMSO, and negligible in water) is significantly stronger than on the green emission band (514 nm in 1,4-dioxane, 513 nm in DMSO, and 508 nm in water), which remains largely unaffected by solvent polarity. This differential solvent effect on emission properties suggests the potential application of compound **1** as a solvent polarity sensor.

The apparent quantum yields of compound **1** in the three solvents at three excitacion wavelenght (350, 470 and 560) are shown in Tables S1 and S2 (see SI-Quantum Yield Calculation). Our data show that quantum yields is dependent of the excitation wavelenght. The calculated values of compound 1 at the wavelenght of 470 nm were 0.444 ± 0.008 in 1,4-dioxane, 0.378 ± 0.007 in DMSO, and 0.18 ± 0.002 in water.

Fluorescence lifetime measurements were performed for compound **1** in the three solvents: DMSO, 1,4-dioxane, and water. The decay profiles were fitted using a triexponential model for DMSO and 1,4-dioxane and biexponential model for water, and average lifetimes were calculated for both emission bands. In DMSO, the average lifetimes were 5.18 ± 0.03 ns for the green band and 1.44 ± 0.07 ns for the red band. In 1,4-dioxane, the lifetimes were 4.83 ± 0.02 ns (green) and 2.81 ± 0.04 ns (red), while in water, the values were 6.43 ± 0.12 ns and 5.79 ± 0.05 ns, for the green and red emission, respectively. The lifetimes and their fractional contributions for each model is provided in the Supplementary Information (see Fig. S1 and Table S3). These results indicate that the green emission exhibits consistently longer lifetimes across all solvents, and its sensitivity to the solvent environment is reflected in the pronounced variation observed. The contrast in kinetic complexity (biexponential in water vs. triexponential in DMSO/Dioxane) is rationalized by the calculated adiabatic S2–S1 energy gap. In water, since anti-Kasha behavior is favored when this gap is greater than 0.5 eV, a large S2–S1 energy gap effectively suppresses the non-radiative S2 \to S1 internal conversion. This suppression minimizes the intermediate kinetic pathways, leading to a simplified decay dominated primarily by the two radiative channels (S2 → S0 and S1 → S0), which can be satisfactorily modeled with a biexponential fit. However, in DMSO and 1,4-dioxane, a smaller energy gap means that the S2 → S1 internal conversion pathway becomes more significant. The involvement of this third, competing kinetic process (IC) introduces greater complexity into the overall relaxation dynamics of the excited states, thereby necessitating a third component for an accurate triexponential fit.

To gain deeper insight into the nature of both emission bands and absorption peaks, we conducted theoretical calculations to elucidate the underlying mechanisms.

3.2. Theoretical insights

DFT and TD-DFT calculations were performed in 1,4-dioxane, DMSO and water solution to rationalize the absorption and photoluminescence spectra of compound **1**. The solvent was treated implicitly using the Polarizable Continuum Model (PCM). The molecular geometry of the ground state (S_0) and two excited states (S_1 and S_2) were optimized at the PBE0/6-31+G**, M06-2X/6-31+G**, CAM-B3LYP6-31+G** and ωB97xD/6-31+G** levels of theory in dioxane, DMSO and water with the aim to characterize the nature of the electronic transitions involved in the excitation and relaxation processes. We tried four different functionals to check the consistency of our theoretical results. The best results in the calculation of the photophysical properties (absorption and emission) were obtained with M06-2X, so the discussion will focus on this functional.

Fig. 3 shows the optimized geometry for the ground state S_0 in 1,4-dioxane using M06-2X/6-31+G** (see Figs. S2 and S3 in the Supporting Information for geometries in water and DMSO). The central carbon skeleton shows almost planar geometry with dihedral angles in the range 1.3–2.4°. The BODIPY platform presents a deviation around 34° from the central skeleton and decreases up to 17° in the first excited state S_1 and 11° in in the second excited state S_2. As regards the dihedral angle

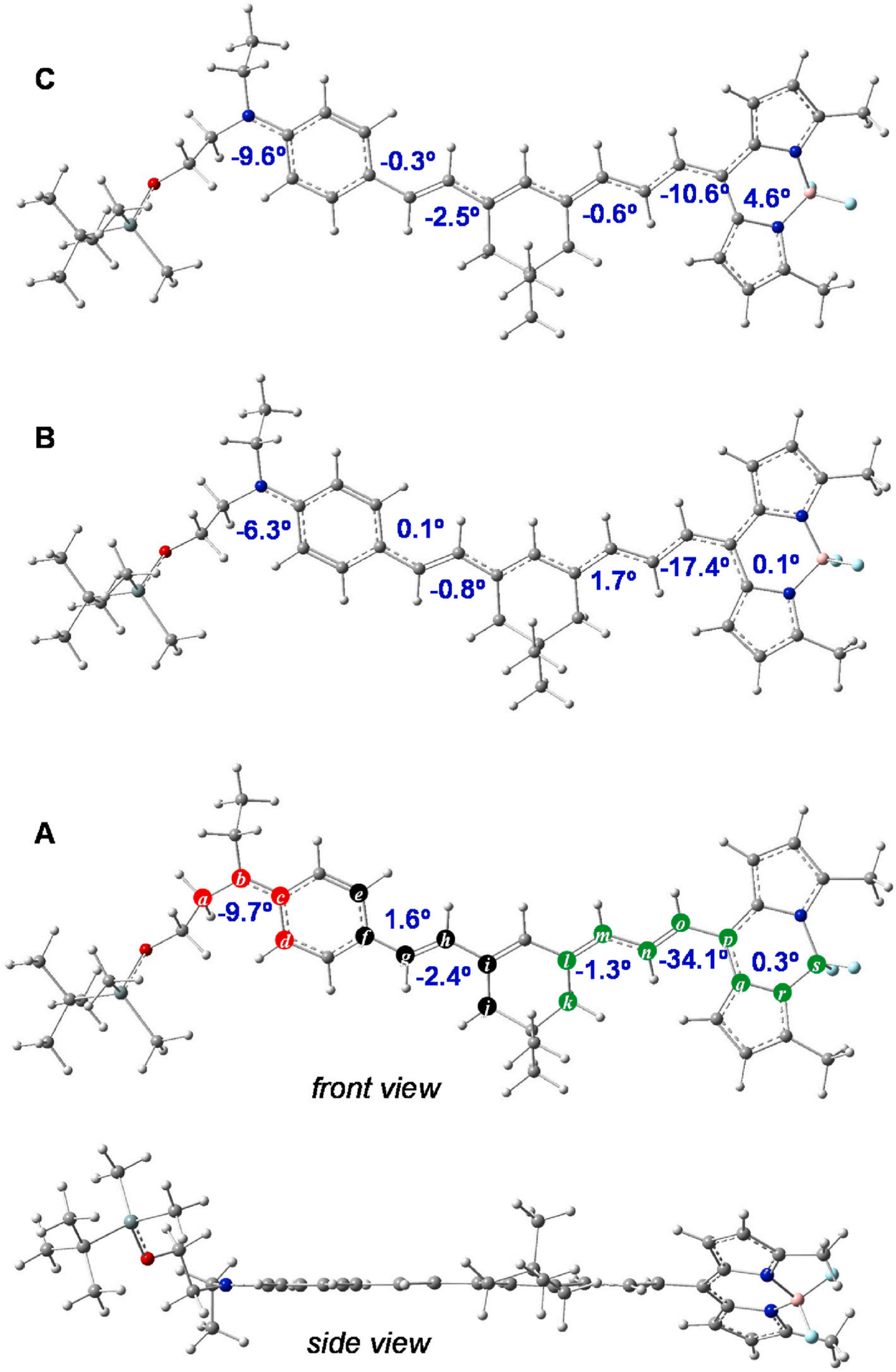

Fig. 3. Selected dihedral angles for (A) ground state S_0, (B) excited state S_1 and (C) excited state S_2 of compound **1** calculated at the M06-2X/6-31+G** level of theory in dioxane solution.

between the donor amine group and the central skeleton, it takes a value of 9.7° in the ground state and decreases up to 6.3° after excitation in S_1 paving the way to the intramolecular charge transfer. However, it hardly deviates from the value in the fundamental state when the molecule reaches the S_2 excited state.

Table 2 lists the predicted dipole moments for compound **1** in different solvents for the ground state S_0 and excited states S_1 and S_2. Taking as reference the ground state (μ_G), the dipole moment doubles after excitation in S_1 while it takes a similar value in S_2 predicting the same trend in the three solvents. In addition, μ_G and μ_{S1} increases with the polarity of the solvent being this effect is more pronounced in S_1 from 20 D in 1,4-dioxane up to 31 D in DMSO and water. These results help explain the greater solvatochromism observed for the more red-shifted emission at 650–670 nm, as well as the weaker solvent effect on the emission at 525 nm, as discussed later.

Table 2
Dipole moments (in Debye) of the compound 1 in S_0 (μ_G), S_1 (μ_{S1}) and S_2 (μ_{S2}) states calculated at the M062X/6-31+G** level of theory in solution.

Solvent	μ_G	μ_{S1}	μ_{S2}	μ_{S1} -μ_G	μ_{S2} -μ_G
Dioxane	12.13	20.19	16.72	8.06	4.59
DMSO	14.42	31.23	16.73	16.81	2.31
Water	14.47	31.54	16.74	17.07	2.27

Table 3 lists the vertical electronic transitions calculated for compound **1** in 1,4-dioxane, DMSO and water solution, along with the experimental data for comparison. TD-DFT calculations are in good agreement with the experimental absorption wavelengths with deviations lower than 0.04 eV for M06-2X, followed by CAM-B3LYP (~0.1 eV) while ωB97xD and PBE0 yield larger deviations, 0.3 and 0.5 eV, respectively. According to the M06-2X theoretical calculations, the main band observed around 540–560 nm could be assigned to the lowest $S_0 \rightarrow S_1$ transition with high oscillator strength values (*f~1.9*), showing a high HOMO→LUMO contribution (≥82 %) and a low contribution of HOMO-2→LUMO (12 %). A second transition $S_0 \rightarrow S_2$ is predicted at 462 nm with high contribution of HOMO-1→LUMO (~90 %) and *f*~0.48. This transition could be below the broadband envelope at 540–560 nm.

The frontier molecular orbitals are represented in Fig. S4. HOMO is delocalized from the donor amine group along the carbon skeleton, while LUMO and HOMO-1 are localized mainly in the BODIPY platform.

Since HOMO and LUMO are involved in the $S_0 \rightarrow S_1$ transition, this transition presents intramolecular charge transfer character and makes it sensitive to the polarity of the surrounding medium. However, the electronic transition $S_0 \rightarrow S_2$ from HOMO-1 to LUMO only involves the BODIPY platform. These results are consistent with experimental observations concerning the different nature of the two observed absorption and emission bands and their dependence on solvent polarity.

A simpler view of electron excitation than shown by canonical orbitals can be obtained by expressing the electronic transition using Natural Transition Orbitals (NTOs) called *hole* and *particle*. The *hole* NTO represents the electron that leaves the occupied orbital upon excitation, while the *particle* NTO represents the excited electron that moves to an unoccupied orbital. λ quantifies the contribution of each specific *hole-particle* NTO pair to the overall electronic transition. Fig. 4 and Fig. S5 show the NTO analysis for the $S_0 \rightarrow S_1$ and $S_0 \rightarrow S_2$ transitions. For the $S_0 \rightarrow S_1$ excitation, the *hole* NTO is placed over the molecular platform involving the amino group, while the *particle* NTO is more localized over the BODIPY moiety with eigenvalues of $\lambda = 0.97$ in water and dioxane. However, for the $S_0 \rightarrow S_2$ transition, *hole-particle* NTO pair is almost exclusively localized over the BODIPY platform with $\lambda = 0.99$.

The molecular geometry of the first S_1 and second S_2 excited states was optimized in solution. Table 4 shows the calculated emission using state-specific solvation approach along with the experimental emission wavelengths for comparison. The M06-2X functional matches well the experimental observations with energy differences of less than 0.2 eV. The results from PBE0, CAM-B3LYP and ωB97xD functionals are shown in Tables S4 and S5. The lowest energy emission band observed at 655nm/670 nm in dioxane/DMSO solution has been assigned to the $S_1 \rightarrow S_0$ transition, with calculated emission wavelengths of 684 nm (dioxane) and 734 nm (DMSO), confirming the red shift with increasing solvent polarity. Regarding the second emission band observed at 525 nm, it is assigned to the $S_2 \rightarrow S_0$ relaxation, which exclusively involves the BODIPY platform. Although the explicit solvation model considering solvent molecules interacting with the fluorophore may be a more realistic solvation model, the good agreement between the experimental and theoretical data shown in Table 4 leads us to conclude that the implicit solvation model using the Polarizable Continuum Model (PCM) works reasonably well in the system studied in this work.

Therefore, the theoretical calculations confirm the two emission bands observed for compound **1**, the distinct electronic nature of the transitions involved, and their dependence on solvent polarity. Additionally, the emission from S_2 excited state would give compound **1** anti-Kasha character which could be tuned with the solvent polarity.

The Anti-Kasha emission refers to luminescence that occurs from an excited state higher than the first excited state. As discussed in previous works [27,51], in general for fluorophores with an adiabatic energy gap between the excited states S_1 and S_2 greater than 0.5 eV, non-radiative deactivation through internal conversion can be suppressed or minimized, allowing radiative relaxation of S_2. Table S6 shows that the calculated values for $\Delta E(S_1 - S_2)$ are 0.9 eV in water and 0.5 eV in dioxane and then Anti-Kasha behavior would be more favored in water than in dioxane. In addition, the reorganization energy, λ, has been calculated to estimate the internal conversion in S_1 and S_2 (see Table S6 and Fig. S6). The predicted values for λ are 0.9 eV (water) and 0.6 eV

Table 3
Experimental maximum absorption wavelengths (λ_{ab}^{exp}) and calculated vertical electronic transitions ($\lambda_{vert\text{-}ab}^{calc}$) (in nm and eV in parenthesis), oscillator strength (*f*), and main components of the $S_0 \rightarrow S_n$ transitions (% contribution) at the TD-CAM-B3LYP/6-31+G** and M06-2X/6-31+G** levels of theory in solution.

Solvent	λ_{ab}^{exp}	$\lambda_{vert\text{-}ab}^{calc}$	Transition	*f*	% Contribution
CAM-B3LYP/6-31+G**					
Dioxane	540 (2.30)	515 (2.41)	$S_0 \rightarrow S_1$	2.03	H → L (77), H-2 → L (16)
		456 (2.72)	$S_0 \rightarrow S_2$	0.50	H-1 → L (92)
	384	353 (3.52)	$S_0 \rightarrow S_3$	0.21	H-2 → L (48), H → L+1 (36)
	305	326 (3.81)	$S_0 \rightarrow S_4$	0.56	H → L+1 (50), H-2 → L (22)
DMSO	550 (2.25)	545 (2.28)	$S_0 \rightarrow S_1$	2.03	H → L (77), H-2 → L (15)
		451 (2.75)	$S_0 \rightarrow S_2$	0.49	H-1 → L (86)
	354	362 (3.42)	$S_0 \rightarrow S_3$	0.13	H-2 → L (54), H → L+1 (22)
	310	333 (3.72)	$S_0 \rightarrow S_4$	0.66	H → L+1 (65), H → L (12)
Water	560 (2.21)	542 (2.29)	$S_0 \rightarrow S_1$	2.01	H → L (77), H-2 → L (15)
		448 (2.77)	$S_0 \rightarrow S_2$	0.47	H-1 → L (85)
	360	361 (3.43)	$S_0 \rightarrow S_3$	0.12	H-2 → L (55), H → L+1 (19)
	310	333 (3.73)	$S_0 \rightarrow S_4$	0.68	H → L+1 (67), H → L (11)
M06-2X/6-31+G**					
Dioxane	540 (2.30)	530 (2.34)	$S_0 \rightarrow S_1$	1.95	H → L (82), H-2 → L (12)
		462 (2.68)	$S_0 \rightarrow S_2$	0.48	H-1 → L (94)
	378	361 (3.43)	$S_0 \rightarrow S_3$	0.09	H-2 → L (64), H → L+1 (21)
	344	336 (3.69)	$S_0 \rightarrow S_4$	0.72	H → L+1 (68), H-2 → L (14)
DMSO	550 (2.25)	561 (2.21)	$S_0 \rightarrow S_1$	1.94	H → L (82), H-2 → L (12)
		458 (2.71)	$S_0 \rightarrow S_2$	0.47	H-1 → L (91)
	354	374 (3.32)	$S_0 \rightarrow S_3$	0.05	H-2 → L (70), H → L+1 (10)
	306	343 (3.62)	$S_0 \rightarrow S_4$	0.77	H → L+1 (80)
Water	560 (2.21)	558 (2.22)	$S_0 \rightarrow S_1$	1.92	H → L (83), H-2 → L (11)
		454 (2.73)	$S_0 \rightarrow S_2$	0.46	H-1 → L (91)
	364	373 (3.33)	$S_0 \rightarrow S_3$	0.05	H-2 → L (71)
	306	342 (3.63)	$S_0 \rightarrow S_4$	0.78	H → L+1 (81)

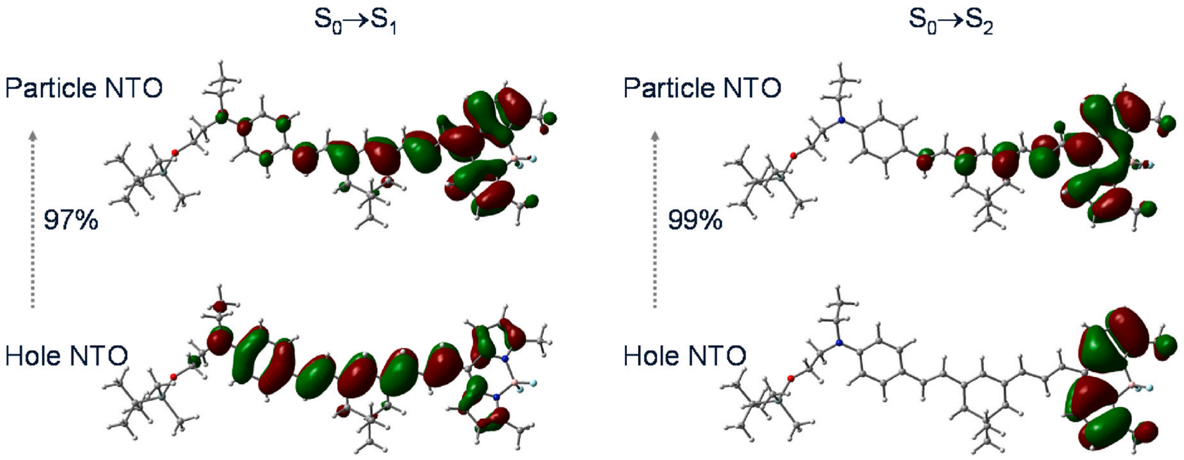

Fig. 4. NTO (isocontour plots 0.02 a.u.) calculated for the compound **1** in water solution at the M06-2X/6-31+G** level of the theory. The value for λ has been included in %.

Table 4
Experimental (λ_{em}^{exp}) and calculated ($\lambda_{vert\text{-}em}^{calc}$) maximum emission wavelength (in nm and eV in parenthesis) for the $S_1 \rightarrow S_0$ and $S_2 \rightarrow S_0$ transitions at the M06-2X/6-31+G** level of theory in solution.

Solvent	λ_{em}^{exp}	Φ_F (%)	Transition	$\lambda_{vert\text{-}em}^{calc}$	f	% Contr.
Dioxane	655(1.89)	44.42	$S_1 \rightarrow S_0$	684 (1.81)	2.55	H → L (95)
	525(2.36)		$S_2 \rightarrow S_0$	541 (2.29)	0.39	H-1→L (92)
DMSO	670(1.85)	37.84	$S_1 \rightarrow S_0$	734 (1.69)	2.80	H → L (96)
	525(2.36)		$S_2 \rightarrow S_0$	500 (2.48)	0.53	H-1→L (94)
Water	–		$S_1 \rightarrow S_0$	734 (1.69)	2.80	H → L (96)
	525(2.36)	18.09	$S_2 \rightarrow S_0$	493 (2.51)	0.54	H-1→L (94)

(dioxane) in S_1, while similar values were found in S_2, 0.4 eV and 0.5 eV, in water and dioxane, respectively. Therefore, the larger reorganization energy in water solution in S_1 could justify the lower quantum yield experimentally measured for compound **1** in aqueous solution due to a larger internal conversion through non-radiative vibrational relaxation.

3.3. Solvent polarity effects on fluorescence

The theoretical approach has elucidated the mechanisms underlying both emission bands and confirmed that solvent polarity affects the two transitions differently. To further investigate the influence of solvent polarity on the fluorescence signal, we selected 1,4-dioxane and water as cosolvents due to their significant difference in polarity, which allows for a wide range of polarity values in the study. We measured fluorescence emission at various proportions of 1,4-dioxane and water using an excitation wavelength of 560 nm (see Fig. 5A) to preferentially excite the $S_0 \rightarrow S_1$ transition, and an excitation wavelength of 470 nm (see Fig. 5B and C) to preferentially excite the BODIPY platform, which is involved in the $S_0 \rightarrow S_2$ transition.

As observed in Fig. 5A, in the 1,4-dioxane:water solvent system, the band corresponding to the $S_1 \rightarrow S_0$ transition exhibits almost negligible fluorescence at 0 %–20 % (v:v) 1,4-dioxane. Between 40 % and 60 % 1,4-dioxane, an emission band centered around 620 nm appears, accompanied by a shoulder around 690 nm. At 80 %–90 % 1,4-dioxane, the shoulder increases in intensity, becoming a distinct peak (λ^{max} = 690 nm at 80 % dioxane). Finally, at 95 %–100 % dioxane, the band at 620 nm disappears, and the band at 690 nm increases in intensity, shifting to a blue-shifted position at 656 nm. Similar trends are observed for the $S_1 \rightarrow S_0$ transition under excitation at 470 nm (see Fig. 5B and C).

Regarding the $S_2 \rightarrow S_0$ transition, the emission band is centered at 525 nm with small variations in the wavelength maximum at different proportions of 1,4-dioxane, as predicted by the theoretical calculations. From 0 % to 20 % 1,4-dioxane, the intensity remains almost constant. However, with the addition of more dioxane (starting at 40 %), the intensity reaches a maximum and then decreases until 95 % 1,4-dioxane. From 95 % to 100 % 1,4-dioxane, the fluorescence intensity of the $S_2 \rightarrow S_0$ transition increases again alongside with the $S_1 \rightarrow S_0$ band in the 650–670 nm range.

Interestingly, excitation at 470 nm reveals both emission bands (Kasha at ~660 nm and anti-Kasha at ~525 nm). As the intensities of these bands are highly dependent on the surrounding environment, we studied the variation in the emission bands through a ratiometric measurement between the wavelengths of 660 nm and 525 nm. The results of this calculation are shown in Fig. 5D. The data indicate that the ratio remains nearly constant from 0 % to 40 % 1,4-dioxane. Beyond this point, the anti-Kasha emission becomes more pronounced, and the ratio begins to increase linearly from 40 % to 95 % dioxane. From 95 % to 100 % dioxane, the ratio value exhibits an exponential increase. Therefore, from 40 % dioxane onward, the ratiometric calculation between the two bands is influenced by the hydrophobicity of the surrounding environment, highlighting compound **1**'s potential as a polarity sensor. The probe's sensitivity is specifically adequate for the biological environment, transforming an apparently narrow ratiometric range into an operational advantage. Since the internal compartments of living cells operate within a critical and limited physiological polarity range, the precise tuning of the linear segment maximizes resolution for detecting subtle variations between distinct cellular, ensuring reliable and specific ratiometric readings for assessing subtle polarity shifts in heterogeneous cellular settings.

To ensure the reliability of Compound 1 for sustained live-cell imaging and dynamic monitoring, its resistance to photobleaching was systematically assayed. The probe demonstrated strong resistance to photobleaching under continuous irradiation over a 30-min period (see Fig. S7). We observed that in water solution, the initial signal decreased by only approximately 15 % after 10 min of continuous exposure. Resistance was even higher in the organic solvents, where the decrease in initial signal was limited to around 5 % in both DMSO and 1,4-dioxane. Crucially, as the dual emission bands (short-wave and long-wave) were affected similarly by the irradiation, the calculated ratiometric values remained almost constant during the entire assay. This high photostability ensures the probe's suitability for reliable and long-

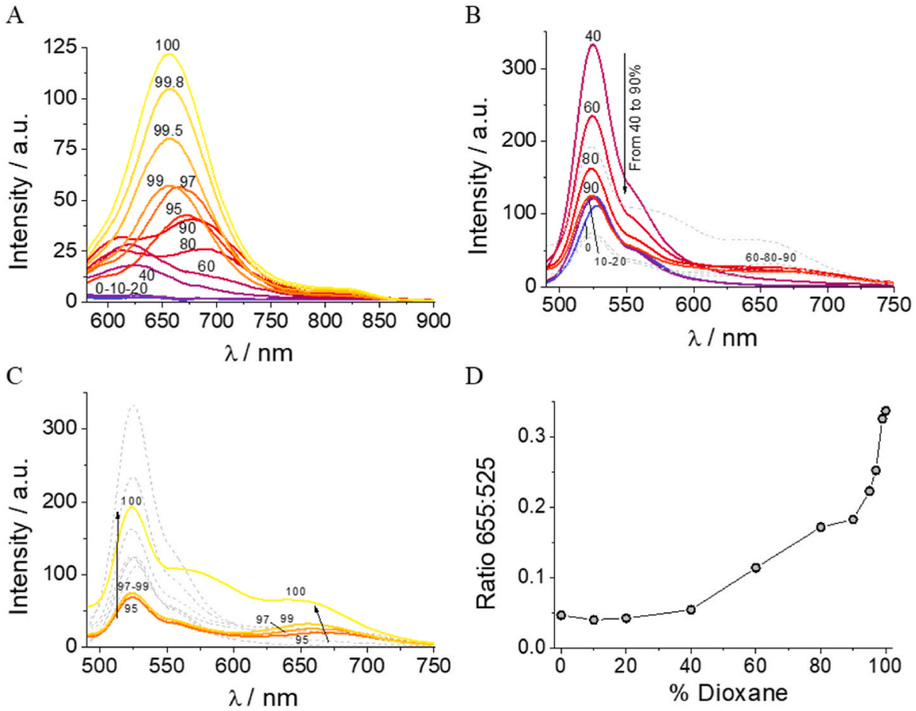

Fig. 5. Experimental fluorescence emission spectra of compound **1** (4×10^{-6} M) in different volume ratios (v:v) of 1,4-dioxane:water at excitation wavelengths of (A) $\lambda_{ex} = 560$ nm, and (B, C) $\lambda_{ex} = 470$ nm. Panel (B) displays the emission spectra for 1,4-dioxane concentrations ranging from 0 % to 90 % (v:v), while panel (C) covers the range from 95 % to 100 % (v:v). (D) Ratiometric calculations at 655 nm and 525 nm for different 1,4-dioxane:water proportions.

term ratiometric measurements.

3.4. Application in live cells

To evaluate the potential biological application of compound **1**, we introduced it to live HeLa cells. Fluorescence intensity was monitored after the addition of compound **1** (see Fig. S8). The fluorescence reached its maximum intensity spontaneously within 10 min, indicating a rapid uptake of compound **1** by the live cells and distinguishing it clearly from the autofluorescence (see Fig. S9). After 10 min of incubation, we measured the fluorescence in two distinct detection channels: the green channel, which captures the emission from the anti-Kasha transition, and the red channel, which detects the emission from the Kasha transition. Cytotoxicity was evaluated after 24 h of incubation. The results revealed a very low toxicity (around 5 %) compared to the control samples (Fig. S10), confirming the biocompatibility of compound 1 under the tested conditions.

Fig. 6 and S10 show representative images from both channels. As observed, compound **1** exhibits differences in fluorescence intensity across various internal structures, with the intensity being stronger in the red channel. In contrast, the green channel displays more homogeneous fluorescence, although the internal structures remain clearly visible. While the intensity differences may be attributed to varying accumulation of compound **1** in different intracellular compartments, the ratiometric measurements between both channels (see Fig. 6A and S10) help eliminate artifacts caused by concentration differences of compound **1**. As previously demonstrated, the ratio value depends on the polarity of the surrounding environment. Therefore, the ratio maps shown in Fig. 6A and S10 provide information on the polarity of the internal structures within the cells. In these images, a false-color representation is used, where blue indicates low ratio values (associated with higher polarity regions) and red indicates high ratio values (corresponding to lower polarity regions).

As the fluorescence intensity varies significantly across different intracellular compartments, these regions can be easily analyzed separately by isolating them. We selected five regions inside the cell: the nucleus, cytosol, nuclear membrane, and two distinct internal structures/organelles differentiated by their fluorescence intensity (internal structures 1 exhibit higher intensity compared to internal structures 2.). In Fig. S11, we show the different regions of interest studied. We then calculated the ratio values in each region and present the histograms in Fig. 6B. The data show that the nucleus exhibits the highest polarity among the regions studied. The second highest polarity is found in the internal regions with homogeneous fluorescence, which we have associated with the cytosol. We also found that the nuclear membrane and internal structures 2 (those with the lowest intensity) present a similar polarity. Finally, the internal structures with higher intensity correspond to the lower polarity observed. These findings demonstrate that the ratio between the two emission bands of this compound can be used to study polarity differences in live cells and present a sensitivity that can distinguish the polarity between cellular compartments. The probe's temporal efficiency is dictated by its inherent photophysical mechanism, where the ratiometric signal relies on the internal competition between the anti-Kasha and Kasha emission pathways, coupled by internal conversion (IC). Polarity shifts instantaneously alter the relative population of S_1 and S_2. The measured fluorescence lifetimes (\tau), determined via TCSPC, exist entirely on the nanosecond (ns) timescale. Because the total process—from excitation to subsequent dual emission—is completed within nanoseconds, the ratiometric signal stabilizes nearly instantaneously following an environmental polarity change, ensuring the probe is highly efficient and sufficiently rapid for real-time monitoring of dynamic biological events, which typically occur on the microsecond [52], millisecond [53], or second scale [54].

4. Conclusion

The experimental and theoretical study of compound 1 in different solvents (1,4-dioxane, DMSO, and water) reveals that its emission and excitation spectra are highly sensitive to solvent polarity. Two distinct emission peaks are observed: one stable at 525 nm across all solvents,

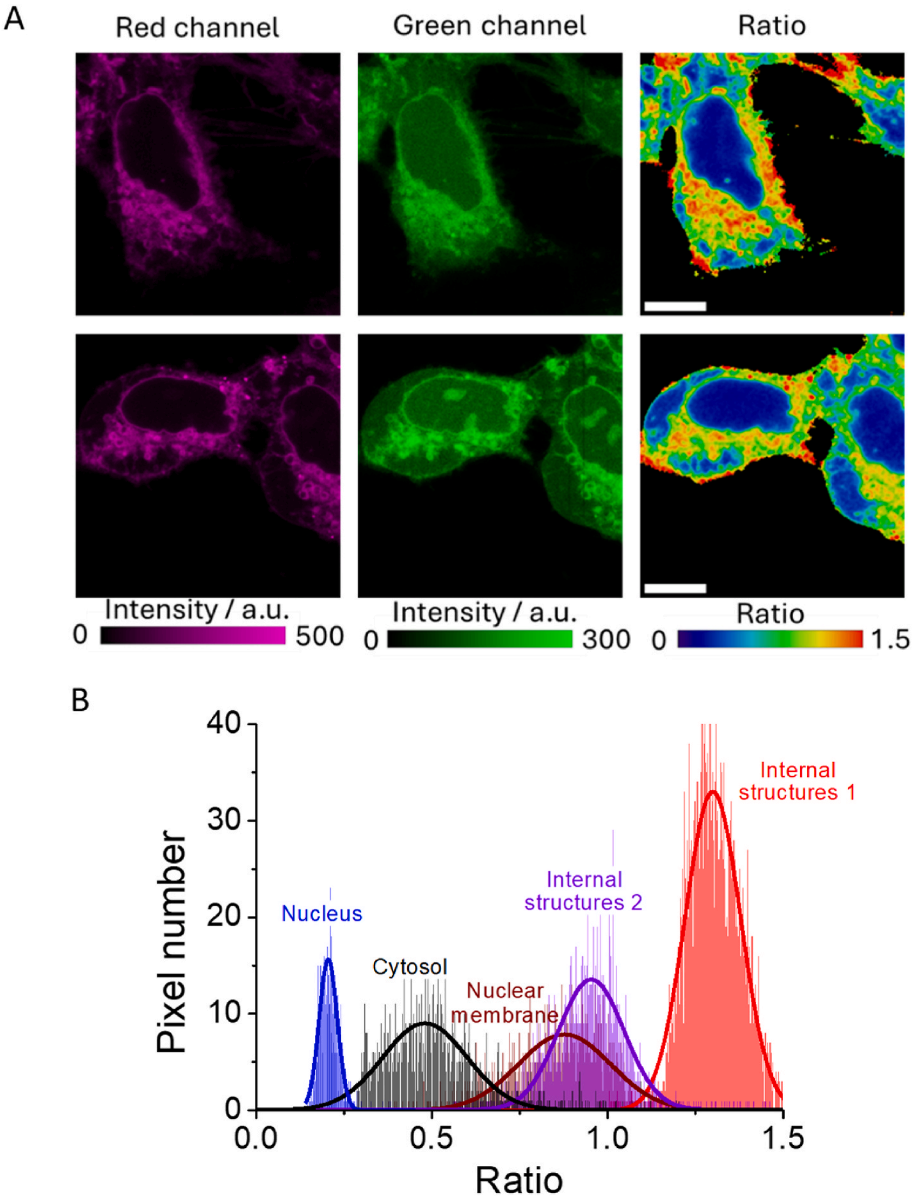

Fig. 6. (A) Fluorescence and ratio images of HeLa cells incubated with 4 × 10^{-6} M of compound **1**. The left panel shows the red channel ($\lambda_{em} = 685/75$), the middle panel displays the green channel ($\lambda_{em} = 509/11$), and the right panel represents the ratio image. Scale bars represent 10 μm. (B) Histograms of the ratio values for the five regions of interest. (For interpretation of the references to color in this figure legend, the reader is referred to the Web version of this article.)

and another that shifts between 656 nm and 690 nm depending on the solvent. TD-DFT calculations confirm that these two emission bands correspond to Kasha (red emission) and anti-Kasha (green emission) transitions, respectively.

In biological applications, compound **1** demonstrates rapid uptake by live HeLa cells and the ability to distinguish between different cellular compartments, indicating its potential as a polarity sensor. Ratiometric analysis of the emission bands (Kasha and anti-Kasha) allows for the elimination of concentration-dependent artifacts, providing reliable data on the polarity of intracellular structures. Ratio maps generated from these measurements offer valuable insights into the polarity of various cellular compartments.

In conclusion, compound **1** proves to be an effective tool for studying polarity variations in live cells, making it a promising candidate for probing the cellular microenvironment and understanding intracellular polarity differences.

CRediT authorship contribution statement

Luis Crovetto: Writing – review & editing, Writing – original draft, Visualization, Validation, Supervision, Investigation, Formal analysis, Conceptualization. **M. Paz Fernández-Liencres:** Writing – original draft, Visualization, Validation, Software, Methodology, Investigation, Formal analysis. **Elena Villegas-Garcia:** Writing – original draft, Visualization, Investigation, Formal analysis. **Jodie Henningway:** Writing – original draft, Visualization, Investigation, Formal analysis. **M. Dolores Giron:** Investigation, Formal analysis. **Ramon Rios:** Writing – original draft, Visualization, Validation, Supervision, Resources, Methodology, Investigation, Formal analysis, Conceptualization. **Amparo Navarro:** Writing – review & editing, Writing – original draft, Visualization, Supervision, Software, Resources, Project administration, Methodology, Investigation, Funding acquisition, Formal analysis, Conceptualization. **Jose M. Paredes:** Writing – review & editing, Writing – original draft, Visualization, Supervision, Resources, Project administration, Methodology, Investigation, Funding acquisition, Formal analysis, Conceptualization.

Notes

The authors declare no competing financial interest.

Declaration of competing interest

The authors declare that they have no known competing financial interests or personal relationships that could have appeared to influence the work reported in this paper.

Acknowledgment

This work was supported by grants PID2023-149650NB-I00 funded by MICIU/AEI/10.13039/501100011033, FEDER, EU, Grant C-CTS-147-UGR23 funded by Consejería de Universidad, Investigación e Innovación and by ERDF Andalusia Program 2021–2027 and Universidad de Jaén Programa Operativo FEDER Andalucia 2021–2027/ Junta de Andalucia-Consejeria de Universidades, Investigacion e Innovacion (Project M.1.B B TA_000722, Grant 2024/00216). A.N. and M.P. Fernández-Liencres acknowledge Junta de Andalucía (PAIDI-FQM-337). We thank the Centro de Servicios de Informática y Redes de Comunicaciones (CSIRC, Universidad de Granada) for providing the computer time that made this work possible.

Appendix A. Supplementary data

Supplementary data to this article can be found online at https://doi.org/10.1016/j.dyepig.2025.113413.

Data availability

The data supporting this article have been included as part of the Supplementary Information. Additional details are available upon request.

References

[1] Tsien RY. Fluorescent probes of cell signaling. Annu Rev Neurosci 1989;12:227–53.
[2] Vicidomini G, Bianchini P, Diaspro A. STED super-resolved microscopy. Nat Methods 2018;15(3):173–82.
[3] Sankaran J, Balasubramanian H, Tang WH, Ng XW, Röllin A, Wohland T. Simultaneous spatiotemporal super-resolution and multi-parametric fluorescence microscopy. Nat Commun 2021;12(1).
[4] Kays I, Chen BE. Tracking and measuring local protein synthesis *in vivo*. Development 2024;151(21).
[5] Bayle V, Fiche JB, Burny C, Platre MP, Nollmann M, Martinière A, et al. Single-particle tracking photoactivated localization microscopy of membrane proteins in living plant tissues. Nat Protoc 2021;16(3):1600–28.
[6] Chang H, Wang JN, Yang Y, Jiang ZY, Chen Y, Lao ZQ. A mitochondria targeted hydrogen peroxide fluorescent probe for monitoring oxidative stress during influenza virus infection. Spectrochim Acta Mol Biomol Spectrosc 2025;334.
[7] Prasad R, Prerna K, Temgire M, Banerjee P, Kumari R, Kundu GC, et al. Molecular engineering of ultrabright biomimetic NanoGhost for site-selective tumor imaging and biodistribution 2025;14(3):2401233.
[8] Ding C, Zhu A, Tian Y. Functional surface engineering of C-Dots for fluorescent biosensing and in vivo bioimaging. Acc Chem Res 2014;47(1):20–30.
[9] Howes PD, Chandrawati R, Stevens MM. Bionanotechnology. Colloidal nanoparticles as advanced biological sensors. Science 2014;346(6205):1247390.
[10] Resa S, Orte A, Miguel D, Paredes JM, Puente-Muñoz V, Salto R, et al. New dual fluorescent probe for simultaneous biothiol and phosphate bioimaging. Chem Eur J 2015;21(42):14772–9.
[11] Telegin FY, Marfin YS. New insights into quantifying the solvatochromism of BODIPY based fluorescent probes. Spectrochim Acta Mol Biomol Spectrosc 2021;255.
[12] Yu AC, Tolbert CA, Farrow DA, Jonas DM. Solvatochromism and solvation dynamics of structurally related cyanine dyes. J Phys Chem A 2002;106(41):9407–19.
[13] Ueno T, Nagano T. Fluorescent probes for sensing and imaging. Nat Methods 2011;8(8):642–5.
[14] Waggoner AS, Stryer L. Fluorescent probes of biological membranes. Proc Natl Acad Sci U S A 1970;67(2):579–89.
[15] Zhang J, Campbell RE, Ting AY, Tsien RY. Creating new fluorescent probes for cell biology. Nat Rev Mol Cell Biol 2002;3(12):906–18.
[16] Kobayashi T, Yamaguchi T, Hamanaka S, Kato-Itoh M, Yamazaki Y, Ibata M, et al. Generation of rat pancreas in mouse by interspecific blastocyst injection of pluripotent stem cells. Cell 2010;142(5):787–99.
[17] Drubin DG, Nelson WJ. Origins of cell polarity. Cell 1996;84(3):335–44.
[18] Xiang G, Huang XY, Wang TJ, Wang J, Zhao GX, Wang H, et al. The impact of sitagliptin on macrophage polarity and angiogenesis in the osteointegration of titanium implants in type 2 diabetes. Biomed Pharmacother 2020;126.
[19] Najafi M, Goradel NH, Farhood B, Salehi E, Nashtaei MS, Khanlarkhani N, et al. Macrophage polarity in cancer: a review. J Cell Biochem 2019;120(3):2756–65.
[20] Espinar-Barranco L, Paredes JM, Orte A, Crovetto L, Garcia-Fernandez E. A solvatofluorochromic dye as a fluorescent lifetime-based probe of β-amyloid aggregation. Dyes Pigments 2022;202.
[21] Espinar-Barranco L, Luque-Navarro P, Strnad MA, Herrero-Foncubierta P, Crovetto L, Miguel D, et al. A solvatofluorochromic silicon-substituted xanthene dye useful in bioimaging. Dyes Pigments 2019;168:264–72.
[22] Gonzalez-Garcia MC, Pena-Ruiz T, Herrero-Foncubierta P, Miguel D, Giron MD, Salto R, et al. Orthogonal cell polarity imaging by multiparametric fluorescence microscopy. Sens Actuators B Chem 2020;309.
[23] González-Vera JA, Lv F, Escudero D, Orte A, Guo X, Hao E, et al. Unusual spectroscopic and photophysical properties of solvatochromic BODIPY analogues of prodan. Dyes Pigments 2020;182:108510. 1-13.
[24] Huang Y, Xin HT, Zhang Y, Yang GY, Li KY, Wang L, et al. A fluorescent probe based on a coumarin-aurone moiety for visualizing polarity changes in lipid droplets under multiple modes. Sens Actuators B Chem 2025;426.
[25] Wang H, Chen GW, Wang HX, Sun R, Ge JF. Fluorescent probes based on aza-Nile Red for visualizing mitochondrial polarity fluctuation. Sens Actuators B Chem 2025;426.
[26] Wang KN, Liu LY, Mao D, Xu SD, Tan CP, Cao Q, et al. A polarity-sensitive ratiometric Fluorescence probe for monitoring changes in lipid droplets and nucleus during ferroptosis. Angew Chem Int Ed 2021;60(27):15095–100.
[27] Gong JY, Wei PF, Liu JK, Chen YC, Zhao Z, Zhao WJ, et al. Polarity-triggered Anti-Kasha system for high-contrast cell imaging and classification. Aggregate 2023;4(2).
[28] Zhang XY, Chen C, Zhang W, Yin N, Yuan B, Zhuang GL, et al. Anomalous anti-Kasha excited-state luminescence from symmetry-breaking heterogeneous carbon bisnanohoops. Nat Commun 2024;15(1).
[29] Shi LM, Yan CX, Guo ZQ, Chi WJ, Wei JL, Liu WM, et al. De novo strategy with engineering anti-Kasha/Kasha fluorophores enables reliable ratiometric quantification of biomolecules. Nat Commun 2020;11(1).
[30] Brancato G, Signore G, Neyroz P, Polli D, Cerullo G, Abbandonato G, et al. Dual fluorescence through Kasha's rule breaking: an unconventional photomechanism for intracellular probe design. J Phys Chem B 2015;119(20):6144–54.
[31] Ziessel R, Ulrich G, Harriman A. The chemistry of Bodipy: a new *El Dorado* for fluorescence tools. New J Chem 2007;31(4):496–501.
[32] Das S, Dey S, Patra S, Bera A, Ghosh T, Prasad B, et al. BODIPY-Based molecules for biomedical applications. Biomolecules 2023;13(12).
[33] Yang J, Fan YS, Cai FJ, Xu X, Fu B, Wang SF, et al. BODIPY derivatives bearing borneol moieties: enhancing cell membrane permeability for living cell imaging. Dyes Pigments 2019;164:105–11.
[34] Loudet A, Burgess K. BODIPY dyes and their derivatives: syntheses and spectroscopic properties. Chem Rev 2007;107(11):4891–932.
[35] Boens N, Verbelen B, Dehaen W. Postfunctionalization of the BODIPY core: synthesis and spectroscopy. Eur J Org Chem 2015;2015(30):6577–95.
[36] Bertrand B, Passador K, Goze C, Denat F, Bodio E, Salmain M. Metal-based BODIPY derivatives as multimodal tools for life sciences. Coord Chem Rev 2018;358:108–24.
[37] Zhou XH, Davies J, Huang S, Luo JD, Shi ZW, Polishak B, et al. Facile structure and property tuning through alteration of ring structures in conformationally locked phenyltetraene nonlinear optical chromophores. J Mater Chem 2011;21(12):4437–44.
[38] Shi ZW, Luo JD, Huang S, Cheng YJ, Kim TD, Polishak BM, et al. Controlled diels-alder reactions used to incorporate highly efficient polyenic chromophores into maleimide-containing side-chain polymers for Electro-Optics. Macromolecules 2009;42(7):2438–45.
[39] Palao E, Agarrabeitia AR, Bañuelos-Prieto J, Lopez TA, Lopez-Arbeloa I, Armesto D, et al. 8-Functionalization of Alkyl-Substituted-3,8-Dimethyl BODIPYs by Knoevenagel condensation. Org Lett 2013;15(17):4454–7.
[40] Schindelin J, Arganda-Carreras I, Frise E, Kaynig V, Longair M, Pietzsch T, et al. Fiji: an open-source platform for biological-image analysis. Nat Methods 2012;9(7):676–82.
[41] Frisch MJ, Trucks GW, Schlegel HB, Scuseria GE, Robb MA, Cheeseman JR, et al. Gaussian 16 Rev. C.01. Wallingford, CT. 2016.
[42] Adamo C, Barone V. Toward reliable density functional methods without adjustable parameters: the PBE0 model. J Chem Phys 1999;110(13):6158–70.
[43] Zhao Y, Truhlar DG. The M06 suite of density functionals for main group thermochemistry, thermochemical kinetics, noncovalent interactions, excited states, and transition elements: two new functionals and systematic testing of four M06-class functionals and 12 other functionals. Theor Chem Acc 2008;120(1–3):215–41.
[44] Yanai T, Tew DP, Handy NC. A new hybrid exchange-correlation functional using the Coulomb-attenuating method (CAM-B3LYP). Chem Phys Lett 2004;393(1–3):51–7.

[45] Chai JD, Head-Gordon M. Long-range corrected hybrid density functionals with damped atom-atom dispersion corrections. Phys Chem Chem Phys 2008;10(44):6615–20.
[46] Cossi M, Rega N, Scalmani G, Barone V. Energies, structures, and electronic properties of molecules in solution with the C-PCM solvation model. J Comput Chem 2003;24(6):669–81.
[47] Tomasi J, Mennucci B, Cammi R. Quantum mechanical continuum solvation models. Chem Rev 2005;105(8):2999–3093.
[48] Cammi R, Corni S, Mennucci B, Tomasi J. Electronic excitation energies of molecules in solution: state specific and linear response methods for nonequilibrium continuum solvation models. J Chem Phys 2005;122(10).
[49] Improta R, Scalmani G, Frisch MJ, Barone V. Toward effective and reliable fluorescence energies in solution by a new state specific polarizable continuum model time dependent density functional theory approach. J Chem Phys 2007;127(7).
[50] Scalmani G, Frisch MJ, Mennucci B, Tomasi J, Cammi R, Barone V. Geometries and properties of excited states in the gas phase and in solution: theory and application of a time-dependent density functional theory polarizable continuum model. J Chem Phys 2006;124(9).
[51] Escudero D, Veys K. Anti-Kasha fluorescence in molecular entities: central role of electron-vibrational coupling. Acc Chem Res 2022;55:2698–707.
[52] Otosu T, Ishii K, Tahara T. Microsecond protein dynamics observed at the single-molecule level. Nat Commun 2015;6.
[53] Hanson JA, Duderstadt K, Watkins LP, Bhattacharyya S, Brokaw J, Chu JW, et al. Illuminating the mechanistic roles of enzyme conformational dynamics. Proc Natl Acad Sci U S A 2007;104(46):18055–60.
[54] Gingras RM, Sulpizio AM, Park J, Bretscher A. High-resolution secretory timeline from vesicle formation at the Golgi to fusion at the plasma membrane in S. cerevisiae. eLife 2022;11.

Luis Crovetto is an Associate Professor at the Department of Physical Chemistry, Faculty of Pharmacy, University of Granada. He holds a PhD in Chemistry from the same university, where he received the Extraordinary Doctorate Award. His research focuses on the development of fluorescent probes and photophysical studies, with international experience at institutions such as KU Leuven and the Max Planck Institute for Bioinorganic Chemistry.

M. Paz Fernández-Liencres is an Associate Professor of Physical Chemistry at the University of Jaén. She earned her PhD in Pharmacy from the University of Granada and is a member of the PAIDI-FQM337 research group. Her work centers on photophysical and transport properties of chemical systems using computational chemistry methods.

Elena Villegas-García is a researcher affiliated with the University of Granada. Her work involves the application of fluorescence techniques to study cellular environments, particularly in the context of disease diagnostics. She has contributed to the development of fluorescent probes for biomedical applications.

Jodie Henningway recently completed her PhD in Chemistry at the University of Southampton, where she focused on the synthesis of birefringent chromophores for optoelectronic applications. She holds an MChem from the University of Warwick and is currently working as an R&D Chemist at MacDermid Alpha. She is a member of the Royal Society of Chemistry.

Maria D. Giron Full Professor at the Department of Biochemistry and Molecular Biology, University of Granada, Spain. She obtained her PhD in Pharmacy in 1988. Her research interests are mainly related: (i) to the search of new compounds with the ability to target proteins involved in different pathologies such as diabetes, obesity or cancer and (ii) the biological characterization of theranostics compounds of importance in biomedicine.

Ramon Rios is a Professor of Chemistry at Khalifa University and former Reader in Organic Chemistry at the University of Southampton. He obtained his PhD from the University of Barcelona and has held postdoctoral positions at MIT, the University of Pennsylvania, and the Max Planck Institute. His research interests include asymmetric synthesis, organocatalysis, and organometallic chemistry. He has authored over 140 publications and several books.

Amparo Navarro is an Associate Professor of Physical Chemistry at the University of Jaén. She earned her PhD in Chemistry from the same institution and is part of the research group on the structure and dynamics of chemical systems. Her expertise lies in vibrational analysis and theoretical spectroscopy.

José M. Paredes is an Associate Professor at the Department of Physical Chemistry, Faculty of Pharmacy, University of Granada. He completed his PhD on xanthene-based fluorescent probes and has worked as a Marie Curie Fellow at the Biophysics Institute (CNR) in Trento, Italy. His research focuses on fluorescence spectroscopy, molecular imaging, and the development of nanoscopic tools for biomedical applications.